IN-93
037465

In -Flight Calibration of the Energetic Gamma-Ray Experiment Telescope (EGRET) on the Compton Gamma-Ray Observatory

J. A. Esposito, D. L. Bertsch, A. W. Chen, B. L. Dingus, C. E. Fichtel, R. C. Hartman, S. D. Hunter, G. Kanbach, D. A. Kniffen, Y. C. Lin, H. A. Mayer-Hasselwander, L. M. McDonald, P. F. Michelson, C. von Montginy, R. Mukherjee, P. L. Nolan, E. Schneid, P. Sreekumar, D. J. Thompson, W. F. Tompkins, and T. D. Willis

Laboratory for High Energy Astrophysics

NASA Goddard Space Flight Center
Greenbelt, MD 20771

In-Flight Calibration of the Energetic Gamma-Ray Experiment Telescope (EGRET) on the Compton Gamma-Ray Observatory

J. A. Esposito [1,2,3], *D. L. Bertsch* [1], *A. W. Chen* [1,4], *B. L. Dingus*[5], *C. E. Fichtel*[1,6], *R. C. Hartman*[1], *S. D. Hunter*[1], *G. Kanbach*[7], *D. A. Kniffen*[8], *Y. C. Lin*[9], *H. A. Mayer-Hasselwander*[7], *L. M. McDonald* [10], *P. F. Michelson*[9] *C. von Montigny*[11], *R. Mukherjee*[12], *P. L. Nolan*[9], *E. Schneid*[13], *P. Sreekumar*[1,2], *D. J. Thompson*[1], *W. F. Tompkins*[9], *and T. D. Willis* [9]

[1]NASA/Goddard Space Flight Center, Code 660, Greenbelt, MD 20771
email at Goddard: Users identified by initials; dlb, awc, rch, sdh, lmm, rch, or djt.
Node: @egret.gsfc.nasa.gov

[2]Universities Space Research Association

[3]Present address: Research and Data Systems Corporation, Suite 104, 7501 Forbes Blvd., Seabrook, MD 20706; email: esposito@mcst.gsfc.nasa.gov

[4]National Research Council Fellow

[5]Department of Physics, University of Utah, Salt Lake City, UT 84112
email: dingus@mail.physics.utah.edu

[6]Retired

[7]Max-Planck Institut für Extraterrestrische Physik, Postfach 1603, 85740 Garching, Germany
email at MPE: Users identified by initials; gok or hrm. Node: @mpe-garching.mpg.de

[8]Hampden-Sydney College, P. O. Box 862, Hampden-Sydney, VA 23943; email: donk@pulsar.hsc.edu

[9]W. W. Hansen Experimental Physics Laboratory, Stanford University, Stanford CA 94305
mail at Stanford: Users identified by initials; lin, pfm, pln, billt, or tdw. Node: @egret1.stanford.edu

[10]Raytheon, NASA/Goddard Space Flight Center, Greenbelt, MD 20771

[11]Science and Computing, GMBH Hagellocher Weg 71 D-72070 Tübingen Germany
email: C.v.Montigny@science-computing.de

[12]Dept. of Physics & Astronomy, Barnard College & Columbia University, New York, NY 10027
email: muk@astro.columbia.edu

[13]Northrop Grumman Corporation, Mail Stop A01-26, Bethpage, NY 11714
email: schneid@egret.gsfc.nasa.gov

ABSTRACT

The Energetic Gamma-Ray Experiment Telescope (EGRET) on the *Compton Gamma-Ray Observatory* has been operating for over seven years since its launch in 1991 April. This span of time far exceeds the design lifetime of two years. As the instrument has aged, several changes have occurred due to spark chamber gas exchanges as well as some hardware degradation and failures, all of which have an influence on the instrument sensitivity. This paper describes post-launch measurements and analysis that are done to calibrate the instrument response functions. The updated instrument characteristics are incorporated into the analysis software.

Subject headings: gamma rays: general - gamma rays: instruments

To be appear in the Astrophysical Journal Supplement Series

1. Introduction

The Energetic Gamma-Ray Experiment Telescope (EGRET) has been operating in space on board the *Compton Gamma-Ray Observatory* (*CGRO*) since the launch and activation in 1991 April. EGRET is one of four instruments on *CGRO* and is sensitive over the energy range from approximately 30 MeV to over 30 GeV, limited at the high end by low counting statistics. Results from the analysis of EGRET data provide important information for understanding a broad range of astrophysical phenomena, including solar flares, pulsars, aspects of our Galaxy and other normal galaxies, gamma-ray bursts, active galaxies, and the extra-galactic diffuse radiation. A summary of the principal findings is given by Fichtel (1996).

The EGRET instrument and its scientific goals have been described by Hughes et al. (1980) and Kanbach et al. (1988 & 1989). The extensive calibration of EGRET prior to launch and during the early part of the mission is described in detail by Thompson et al. (1993), including the calibration at the Stanford Linear Accelerator Center (SLAC), the test for proton-induced background at Brookhaven, and the calibration at the Bates Linear Accelerator. The pre-launch calibration, together with the extensive software developed by the EGRET instrument team, provides the basis for an analysis of the EGRET data, but changes in instrument performance require in-flight calibration information to update the pre-flight calibration results.

The purpose of this paper is to describe the in-flight calibration of the instrument based on observations made throughout the mission, and to address necessary time-dependent corrections to the EGRET pre-flight calibration. Because of the unexpected long lifetime of EGRET, the counting statistics for the diffuse gamma radiation far exceed the statistics obtained during the calibration. The observed intensity of the diffuse emission early in the mission before the instrument performance degraded, and at times following gas refills, serve as a standard for comparing later observations of the diffuse emission and thereby determining the time variability of the instrument response. The point-spread function (PSF) of the instrument is monitored using data from the strong pulsars. For these measurements, only photons whose arrival times are nearly in phase with the pulsar's peak emission are used to increase the signal-to-noise ratio.

A brief summary of the principal features of the instrument and its history is given in the next section to aid in understanding the details the in-flight measurements of the effective area and point-spread functions that are discussed in sections 3 through 5. Section 6 describes the reduced field-of-view (FOV) modes that were implemented at the beginning of Cycle 5 to conserve the remaining spark chamber lifetime, and Section 7 provides information on the major source of EGRET background, the Earth-limb albedo.

2. The EGRET Instrument

The description of the EGRET instrument and the *CGRO* spacecraft will be limited to that necessary for an understanding of this paper. Further details on EGRET may be found in the articles mentioned in the introduction. EGRET is shown schematically in Figure 1. The central element is a multi-level spark chamber that is triggered by a directional scintillator coincidence system. A NaI(Tℓ) Total Absorption Shower Counter (TASC) is situated below the spark chamber to measure the event energy. The upper portion of the instrument is covered by a scintillator dome that is used in anti-coincidence with the triggering system to veto charged particles. EGRET is similar to, but much larger than, the successful SAS-2 (Derdeyn et al. 1972) and COS-B (Bignami et al. 1975) gamma-ray telescopes of the 1970's.

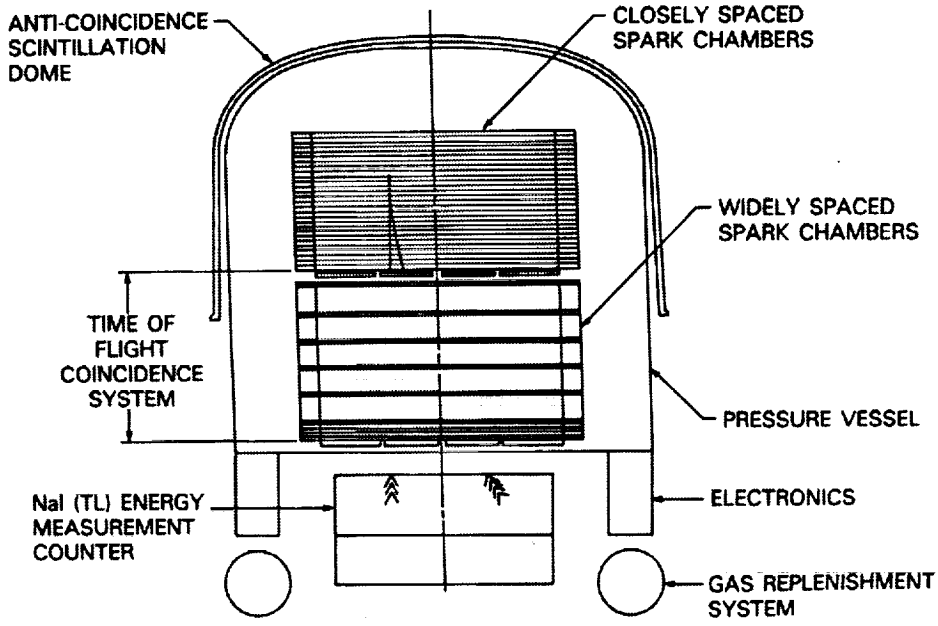

Fig.1 – Schematic diagram of the EGRET instrument.

Gamma rays are detected through the electron-positron pair production interaction in tantalum foils interleaved with the spark chambers tracking layers(decks). The electron or positron may trigger the coincidence system, consisting of a 4 × 4 array of plastic scintillator tiles situated below the lowermost conversion foil, and a similar array at the bottom of the tracker. Of the 256 possible coincidences of an upper tile and a lower tile, 96 are potentially allowed by the EGRET electronics. These 96 coincidences generally are the ones

in which the lower tile is directly below its corresponding upper tile, or its nearest neighbor. Four exceptions are the corner diagonal combinations, which are not allowed because more support structure is in the incident path. The allowed combinations of coincidence tiles are dynamically controlled in orbit to minimize the recording of earth albedo gamma rays. Throughout almost the entire mission, EGRET has been configured to require a third coincidence signal from the TASC. An event trigger is produced by a coincidence signal, together with a time-of-flight signature measured between the two scintillator planes indicating downward-moving particles, and lack of a signal from the anti-coincidence dome covering the instrument. The anti-coincidence system prevents triggering on charged particles, which are much more intense ($\times 10^3$ or more) than the gamma rays.

When a trigger occurs, the spark-chamber high-voltage pulse is generated to record the tracks, and the readout of the spark chamber and event energy data commences. The recorded spark-chamber picture, energy information, gamma ray arrival time, and ancillary information are transmitted to the ground as one "event". Because there are many more events than useful gamma-ray detections, the data analysis system must select the subset of all events that are unmistakably recognized as gamma-ray produced pairs, and from these extract the arrival direction and energy of each detected gamma ray. This procedure is described in Thompson et al. (1993).

The TASC calorimeter consists of 36 NaI(Tℓ) blocks, optically coupled to form a monolithic scintillator (Hughes et al. 1986). It is viewed by 16 photo-multiplier tubes (PMTs) through a light-diffusion box, which helps to equalize the amount of light received by each PMT. The 16 PMTs are divided into two interleaved groups of eight. An analog sum of each group of eight PMT signals is fed into a pair of pulse-height analyzers (PHAs), one for the low-energy range (1 – 200 MeV) and one for high energies (20 MeV to 30 GeV). The two high-energy PHA results are telemetered individually for each triggered event. The two low-energy PHA results are added digitally on-board and accumulated in spectra.

The EGRET instrument was originally designed for a two-year mission. As of 1998 September, EGRET has been in operation for more than seven years, far surpassing the original goal. As the instrument aged, a steady degradation of efficiency and some hardware failures have occurred. A chronological list of gas refills, hardware failures and other major occurrences since the activation of EGRET is given in Table 1. A single triggering tube in the lower scintillator plane failed during 1994 November, reducing the total effective area by $\sim 6\%$, and it also produced an azimuthal asymmetry in the instrument response. Two additional triggering tubes have shown significant gain shifts after 1997 August 3 and 1998 July 7 but these changes produce only minor decreases in the effective area.

The EGRET spark chamber array is composed of two interleaved stacks, called A-stack

and B-stack, with separate high-voltage and readout systems in order to minimize the impact of a component failure. The B-stack displayed a steady decrease in spark efficiency since EGRET activation, and it failed completely in 1997 November. Because of this failure, gaps occur in the electron and positron tracks that complicate the identification of the pair interaction in many cases, and especially at low energies.

The gas used in the EGRET spark chambers (99.5% neon, 0.25% argon, and 0.25% ethane) becomes contaminated by breakdown of ethane by spark chamber firings and to a small degree by residual out-gassing of contaminants. This leads to a slow degradation of spark chamber efficiency that also reduces the capability to identify pair interaction events. A gas purging and refill system capable of five gas exchanges was included in the instrument design. As the spark chamber efficiency degraded, the spark chamber gas was purged and refilled at the dates shown in Table 1. The fifth and last complete gas exchange was performed in 1995 September. After the last two gas exchanges, the spark chamber efficiency was recovered to a somewhat lower maximum level. In order to lengthen the instrument life, EGRET was designed with two independent gas circulation systems to mix the gas uniformly within the pressure vessel. The first gas circulation system failed at nearly three years into the mission and the second gas circulation system continued to work well until its failure in late 1997 (see Table 1). By then, EGRET was being operated at a much lower average trigger rate so the mixing was not so necessary.

3. Effective Area Studies

The time and energy dependence of the instrument's effective area due to the aging effects discussed above are conveniently described (and applied in analysis) in terms of scale factors that multiply the effective area functions that were determined in pre-flight calibration measurements at accelerators (Thompson et al. 1993). In this context, the true effective area, $A(\theta, \varphi, E, t)$ is given by

$$A(\theta, \varphi, E, t) = A_0(\theta, \varphi, E) \times S(E, t) \tag{1}$$

where θ and φ are the polar and azimuthal arrival angles in the spark chamber, E is the gamma ray energy (or energy range) of the observation, t is the mission time since activation, $A_0(\theta, \varphi, E)$ is the effective area as calculated from the pre-flight calibration measurements, and $S(E, t)$ represents the derived scale factors. The factors, $S(E, t)$, might also be functions of the arrival angles, especially if $\theta > 25°$. Efforts to determine if angle is important have been limited by statistics, but the indications are that the dependence is small at angles

Table 1: Significant Instrument Events

Date	Event
04/15/91	Began Instrument Activation and Testing
05/16/91	Began Science Operations Cycle 1
07/15/91	Adjusted the TASC Tube Gains
12/03/91	Replaced Spark Chamber Gas (Fill No. 1)
04/01/92	*CGRO* Tape Recorders Failed, Start Extended Real-Time Coverage
11/17/92	Started Viewing Cycle 2
12/04/92	Replaced Spark Chamber Gas (Fill No. 2)
01/29/93	Adjusted the TASC Tube Gains
06/15/– 06/17/93	Orbit Re-boosted
08/17/93	Started Viewing Cycle 3
11/19/– 11/23/93	Orbit Re-boosted
12/15/– 2/17/93	Orbit Re-boosted
02/09/94	Replaced Spark Chamber Gas (Fill No. 3)
10/04/94	Started Viewing Cycle 4
03/11/94	Gas Circulation Pump Failed
10/28/94	Coincidence Tube C43 Failed
11/02/94	Replaced Spark Chamber Gas (Fill No. 4)
10/03/95	Started Viewing Cycle 5 Began Narrow Angle Mode as the Primary Configuration Implemented Auto-Trigger to Wide Angle for BATSE Burst
04/19/95	Adjusted the TASC Tube Gains
09/07/95	Replaced Spark Chamber Gas(Fill No. 5). Last complete fill
10/15/96	Started Viewing Cycle 6
03/24/ – 04/01/97	Orbit Re-boosted
05/28/– 06/14/97	Orbit Re-boosted
08/06/97	Circulation Pump 2 Failed
10/03/97	Coincidence Tube B24 Rate Reduced
11/04/97	Spark Chamber B (Interleaved stack B) Failed
11/11/97	Started Viewing Cycle 7
07/07/98	Coincidence Tube B44 Rate Reduced

below 25° from the instrument axis. The azimuthal dependence is expected to be even smaller if not completely negligible since the azimuthal dependence in $A_0(\theta, \varphi, E)$ is weak.

3.1. Time Dependence

There are no onboard calibration sources for EGRET, so it is essential to select steady gamma-ray sources on the sky for calibration purposes. The two most promising sources are diffuse emission and gamma-ray pulsars. The strong diffuse emission seen arising from the galactic disk is well understood to result from the interaction of the galactic cosmic rays with the interstellar matter and radiation (Bertsch et al. 1993). This is a steady source of gamma rays since the contribution from time-variable unresolved point sources to the observed diffuse emission is small (Hunter et al. 1997). Of all the currently known gamma-ray point sources (Hartman et al. 1998), the pulsars show the smallest variability in the observed gamma-ray intensity with time (Ramanamurthy et al. 1995; McLaughlin et al. 1996).

Since the pulsars are not within the instrument field-of-view (FOV) during all observations, the more widely distributed diffuse gamma-ray emission is a better calibrator to monitor changes in the instrument sensitivity. The bright Crab, Vela, and Geminga pulsars provide a secondary calibration reference. The scale factors for a given observing period are determined by comparing the diffuse intensity derived from the observation with the intensity obtained from a "standard map". Here the "standard map" refers to an all-sky map of the diffuse gamma-ray emission constructed from a maximum likelihood analysis of data taken from many observation periods near the beginning of the mission, and immediately after the first three gas refill operations when the instrument sensitivity was expected to be similar to the pre-launch sensitivity.

The "standard all-sky map" was made as follows. A comprehensive model of the expected diffuse gamma-ray emission from the Galaxy on $0.5° \times 0.5°$ sky bins was constructed using data on the distribution of matter in the interstellar medium. Detailed discussions are given on the galactic disk component by Bertsch et al. (1993) and Hunter et al. (1997), and on the high galactic latitude component by Sreekumar et al. (1998). Although this model agrees very well with the large-scale longitude and latitude distributions of the observed diffuse emission (Hunter et al. 1997), the model under-predicts in certain regions of the sky (Sreekumar et al. 1998). To allow for imperfections in the model, a localized linear scaling of the input diffuse model was constructed using a likelihood analysis program (Mattox et al. 1996) as follows:

$$B_L(l,b,E) = G_m(l,b,E) \times I(l,b,E) + G_b(l,b,E) \quad (2)$$

where $G_m(l,b,E)$ scales the input diffuse model, $I(l,b,E)$, and $G_b(l,b,E)$ represents a constant background emission that can be identified with an extra-galactic emission, necessary to fit the observations. The $G_m(l,b,E)$ and $G_b(l,b,E)$ factors were determined after accounting for all resolved point sources on the sky. The above analysis was carried out using data taken during periods when the spark-chamber sensitivity was believed to be consistent with pre-flight estimates. These include early observations in Cycle 1 and those immediately following the first three gas exchanges.

A similar scaling of the input diffuse model can be made using data from any observation period during the mission. Ratios of the likelihood model for the observing period and the "standard all-sky map" can be made at all pixels within the FOV of the observation. The mean of a Gaussian fit to the distribution of pixel ratios is taken to be the scale factor appropriate for the given energy and time interval defined by the data. Figure 2 shows the scaled intensity ratio, $S_{E>100}(t)$, for the energy range $E > 100$ MeV from individual observation periods before and after including the scale factor corrections for Cycles 1 through 4. Gas exchange interval 1 (the time interval between activation and gas exchange 1) and gas exchange interval 2 (the time interval between gas exchange 1 and 2) required only small corrections while gas exchange intervals 4 and 5 show the largest corrections to the pre-flight sensitivity.

It is clear from Figure 2 that there is scatter in the observed ratio before and after the scaling correction. The assumption inherent in this analysis is that the performance of EGRET does not vary on short time scales but only over the long term. The extended testing time prior to launch (Thompson et al. 1993) supports this assumption, as does the observed stability of temperatures, voltages, rates, and other on-board status indicators. This approach to correcting the sensitivity differs somewhat from that used for the smaller COS-B instrument (Strong et al. 1987), where known performance changes (especially of the high voltage pulser) produced short-term performance variations as well as a longer-scale degradation.

3.2. Energy Dependence

The scale factors are expected to be energy dependent since the inefficiency of the individual spark-chamber decks affects the selection of low energy events ($E < 300$ MeV) more than the high-energy events. It is possible that the energy dependence could vary between

gas exchange intervals. However, due to the limited number of individual observations during each gas interval and reduced statistics when considering small energy ranges, only the average energy dependence, derived from the combined data from gas exchange intervals 1 through 5 were examined. After the implementation of the derived scale factors, significant changes in the energy dependence between different gas exchange intervals could be

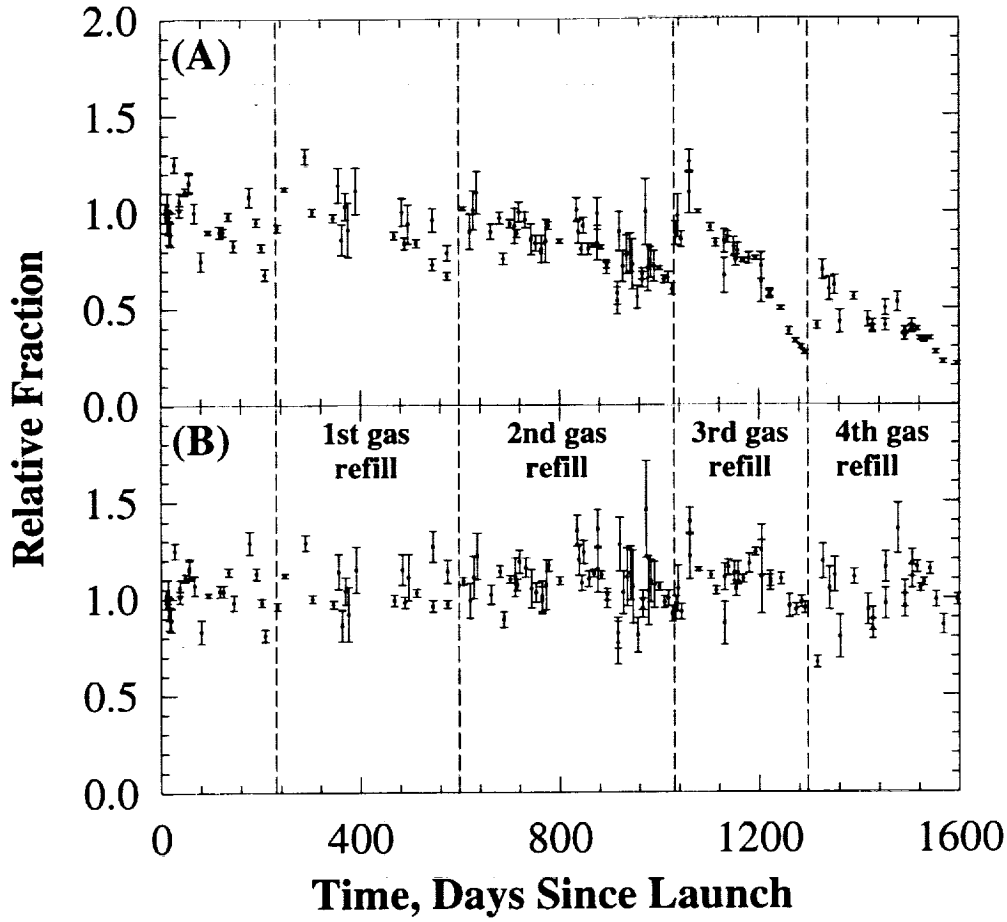

Fig. 2 – Time profile of the efficiency relative to the "standard map", $S_{E>100}(t)$, for $E > 100$ MeV based on the diffuse radiation as observed (A), and after application of the scaling correction (B). Launch (1991 April 7) was on truncated Julian day 48353.

determined using diffuse emission and pulsar spectra from observations spread throughout Cycles 1 through 4.

Photons with $E > 100$ MeV, together with photons from the four wide energy ranges above 30 MeV ($30 < E < 100$ MeV; $100 < E < 300$ MeV; $300 < E < 1000$ MeV; $E > 1000$ MeV), were used to study the energy dependence of the scale factors. Since there are significant numbers of photons from individual observations for $E > 100$ MeV, that selection was used to determine (as discussed in Section 3.1) the time dependence of the $E > 100$ MeV scale factor for all observations. For the four wide energy ranges, statistical limitations permitted the derivation of scale factors only for those extended observations (≥ 2 weeks) with significant exposure to the galactic plane. Correlations derived between the $E > 100$ MeV scale factor, $S_{E>100}(t)$ and those derived for each of the four wide energy ranges were used to characterize the scale factor for any energy and time as

$$S(E,t) = 1.0 + \{2.18 - 0.52\log_{10}(E)\} \times \{S_{E>100}(t) - 1.0\} \quad (3)$$

The above expression provides the scale factor for any energy and time if the corresponding $E > 100$ MeV scale factor is known. After the implementation of these energy- and time-dependent scale factors, it was shown that the pulsar spectra (Fierro et al. 1998) as well as the diffuse emission spectra from different regions of the sky, yield consistent values over Cycles 1 through 4. This cross-check also showed no evidence for significant changes in the energy dependence among different gas exchange intervals. The archival EGRET data for times through the end of Cycle 4 have been corrected using the derived scale factors. Presently, data for Cycles 5 and beyond are being reprocessed.

The scale factors are tabulated for each viewing period as a function of energy in a supporting file that is read by the likelihood analysis and spectral fitting programs. This file is maintained along with the analysis software on both the EGRET computer cluster and at facilities at the Compton Observatory Science Support Center. EGRET exposure and intensity maps already include these factors and an entry in their header quotes the value used in the map. Investigators who obtain analysis and data deliveries from the Science Support Center are also given a file of these values.

3.3. Individual Gamma Ray Adjustments

Early in the mission, two spark chamber readout problems were noted that had a small effect on the electron-positron track pictures in the spark chamber. One was a regular pattern with every $16th$ address (with no adjacent cores) being set on certain spark chamber decks,

and the other was a set of sparks occurring irregularly near the edge of the active area on a number of decks. The regular patterns are easily removed in software before event analysis. Edge spark effects were eliminated by ignoring a small region near the edge of the chamber, which results in a loss in instrument effective area of less than 3%. Correction for this effect has been included in the time-dependent scale factors described above.

Both the ground calibration data and the early flight data showed evidence of a small radial offset of measured source positions from true positions, with the offset being larger for sources at larger angles to the detector axis (Thompson et al. 1993). Although this so-called "fisheye" effect is measurable only for sources with high statistics, it was decided to apply a correction to the arrival direction of each photon to compensate for the offset. The correction moves the arrival direction outward from the detector axis by

$$\theta_{new} = \theta_{orig} \times (1 + a) \tag{4}$$

where θ is the arrival angle in degrees with respect to the EGRET axis and a is the energy-dependent correction factor shown in Figure 3. This correction, derived from a detailed analysis of the pre-flight calibration data, replaces the preliminary one given by Thompson et al. (1993), which was based primarily on early flight results. Because this correction is applied to the photons individually, no further correction is needed in the data analysis.

3.4. Other Calibration Issues

Willis (1996), in his study of the diffuse extra-galactic background seen by EGRET, carried out a detailed study of possible instrumental effects on the diffuse analysis. His method was to use the large-scale diffuse model as a reference source, then map the difference between the observed radiation and the model into an instrument-based coordinate system. The combination of many observations with many different celestial pointing directions assured that no sources or features in the gamma-ray sky would distort the uniformity in instrumental coordinates. A normalized residual was constructed for each point in the instrument field of view. Figure 4 shows a normalized residual map for the energy range > 100 MeV. At any point, the residual R is given by

$$R = (Observed\ counts - Expected\ counts)/Expected\ counts \tag{5}$$

where the expected counts are derived from the high-latitude radiation model. In these instrumental coordinates, COMPTEL is located toward the bottom of the figure.

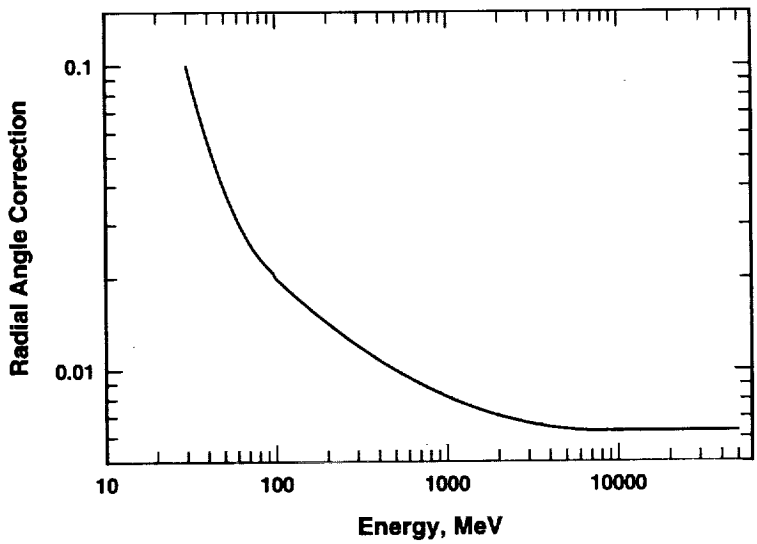

Fig. 3 – Correction for distortion of the angle between the true gamma-ray event arrival and the instrument axis as a function of energy. The EGRET analysis software corrects the incident polar angle of each event by a factor of $1 + a$ where a is given in this plot. See Equation 4.

These residuals show two features. The residuals are not azimuthally uniform or even symmetric. "Hot spots" 20% brighter or 10% dimmer than the average are seen in some directions near the edge of the field of view (taken to be at an inclination angle of 40° to the instrument axis). Secondly, at inclinations between 15° and 25°, some excesses of nearly 20% are seen at azimuthal angles of 45° to the instrument X and Y axes. The asymmetry is attributed to the fact that the original EGRET calibration was carried out only in one octant of the instrument due to time constraints. It seems likely that the instrument response is not perfectly uniform from one octant to another.

Another aspect of the EGRET analysis is also partially responsible for the residuals being larger for higher inclination angles. The individual photons arrival directions are corrected for the "fisheye effect", as described above. This correction ensures that source locations are measured correctly at all inclinations. Because the correction is larger for photons with higher inclination, the effect is to cause a small distortion in the shape of the point-spread function. The background model, however, is convolved with the undistorted

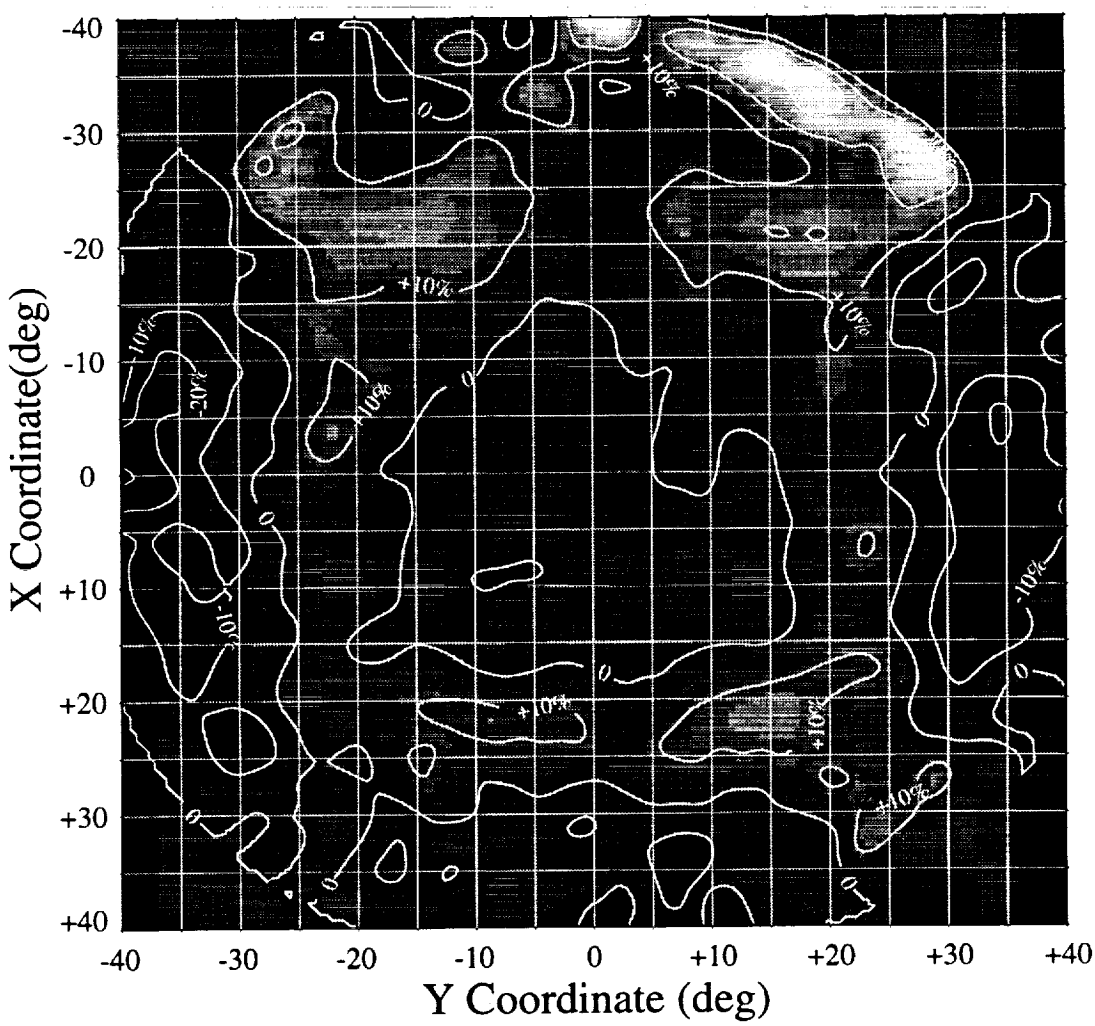

Fig. 4 – Normalized difference map of the observed and modeled diffuse emission, in instrument coordinates. The top of the map represents the $-X$ spacecraft coordinate (facing space); the bottom represents the $+X$ direction (toward COMPTEL and OSSE).

PSF in order to have general applicability. The conversion from counts to intensity after subtracting the background model, then, has some excess at higher inclinations. Modeling by Willis (1996) indicates that most of the observed residual features can be explained by

this hypothesis. For special cases, convolving the background model with the distorted PSF for a given observation could reduce the uncertainty.

For most analyses the effect of these residuals is small, because the regions of deviation from uniformity occupy only a small fraction of the solid angle, mostly at large inclinations, where the statistical uncertainties in EGRET measurements are as large or larger than the residuals. The principal effect this calibration uncertainty has on the results is to contribute to the systematic uncertainty attached to the absolute value of any source flux. This systematic uncertainty was estimated to be in the range from 10% (Thompson et al. 1995) to 13% (Sreekumar et al. 1998), based on the scatter of the individual viewing period normalization values (Fig. 2). McLaughlin et al. (1996) found that at least a 6% systematic uncertainty was needed to give a reasonable statistical measure of non-time variability for the gamma-ray pulsars.

The errors typically quoted for EGRET sources (e.g., The Third EGRET Catalog, Hartman et al. 1998) do not include the systematic error. Instead, they are statistical errors that are given by the standard likelihood analysis (Mattox et al. 1996). An independent analysis of the errors given by the likelihood analysis was done using bootstrap sampling (Simpson & Mayer-Hasselwander 1985) on several sources and the results confirm that the reported values are reasonable.

4. Point-Spread Function (PSF) Studies

4.1. The PSF for Angles $< 20°$ from the Instrument Axis

The EGRET angular dispersion, or point-spread function, was calibrated before launch as a function of energy and direction, and these results were shown by Thompson et al. (1993) to be consistent, within uncertainties, with the early observations of the Crab pulsar. More detailed analysis has also used the Vela pulsar, which is brighter than the Crab and is located in a region of the sky with fewer nearby sources, and for the Geminga pulsar. By employing the well-known ephemerides of these three pulsars and the excellent event time resolution of the instrument, photons that arrive during the pulsar peak times were separated from the off-peak arrival times in order to minimize the influence of background (diffuse) photons. This selection was done in all viewing periods in which the pulsars were in the field of view. Both sets of photons were sorted by angular distance from the source position. Then by summing over different viewing periods, dividing by exposure multiplied by the pulsar phase fraction, and subtracting off-peak from on-peak intensities, the background-subtracted in-flight PSF was constructed. This analysis was repeated for sets of data selected by energy

range, by the angle between the source position and the telescope axis, and by the *CGRO* observing cycle (1 & 2 vs. 3 & 4).

In order to compare the flight data to the calibration model, it was necessary to construct composite point-spread functions from the mono-energetic calibration data. In the initial attempts, a simple power law with index -1.62 was used to represent the Vela spectrum. A good agreement between the flight data and the calibration model was obtained for energies up to 1 GeV, but at higher energies, the flight data profiles were wider than the model prediction. However, when the Vela spectrum was modeled with a broken power law having an index of -2.7 above 1 GeV (which more accurately fits the observed Vela spectrum), the high energy effect was reduced to negligible level.

Figure 5 shows the comparison between the in-flight PSF results and the PSF derived for Vela using the pre-flight calibration data for two energy ranges, $E > 100$ MeV and $E > 1$ GeV respectively. In this plot, only data taken within 25° of the instrument axis were used. The SLAC calibration PSF values appear to match the in-flight data for all energies within the statistics of the pulsar observations used as a reference. Since the pulsars are the brightest sources, this conclusion applies to all sources.

4.2. The PSF for Angles > 20° OFF-AXIS

The EGRET calibration data indicate that the PSF degrades beyond an inclination angle of 20°. Between 20° and 25° off-axis, the effect is almost always negligible, and it can usually be ignored out to 30°. For off-axis angles > 30° however, the effect increases rapidly. PSF calibration files are available out to 40° off-axis, and must be used if accurate fluxes and source significance is to be obtained beyond 30°.

Because of the implications for computational complexity, the EGRET likelihood program does not currently handle the PSF deterioration beyond 30° completely correctly. It does have some limited capability for analysis of a far-off-axis source, by assuming over the entire map the proper PSF for the specific source in question. It cannot simultaneously analyze (correctly) an entire map for sources both close to and far from the axis. For summed maps, in which two or more observations of a specific object have been made at different off-axis angles (not all within 30° of the axis), a time-weighted, angle-dependent PSF would have to be constructed for every point in the map. It is for this reason that the all-sky maps generated by the EGRET Team utilize only those photons within 30° of the EGRET axis. It must be noted that, for axial angles beyond 30°, the EGRET effective area is less than 10% of that on-axis, so there is little loss in the source sensitivity by making the angle cut.

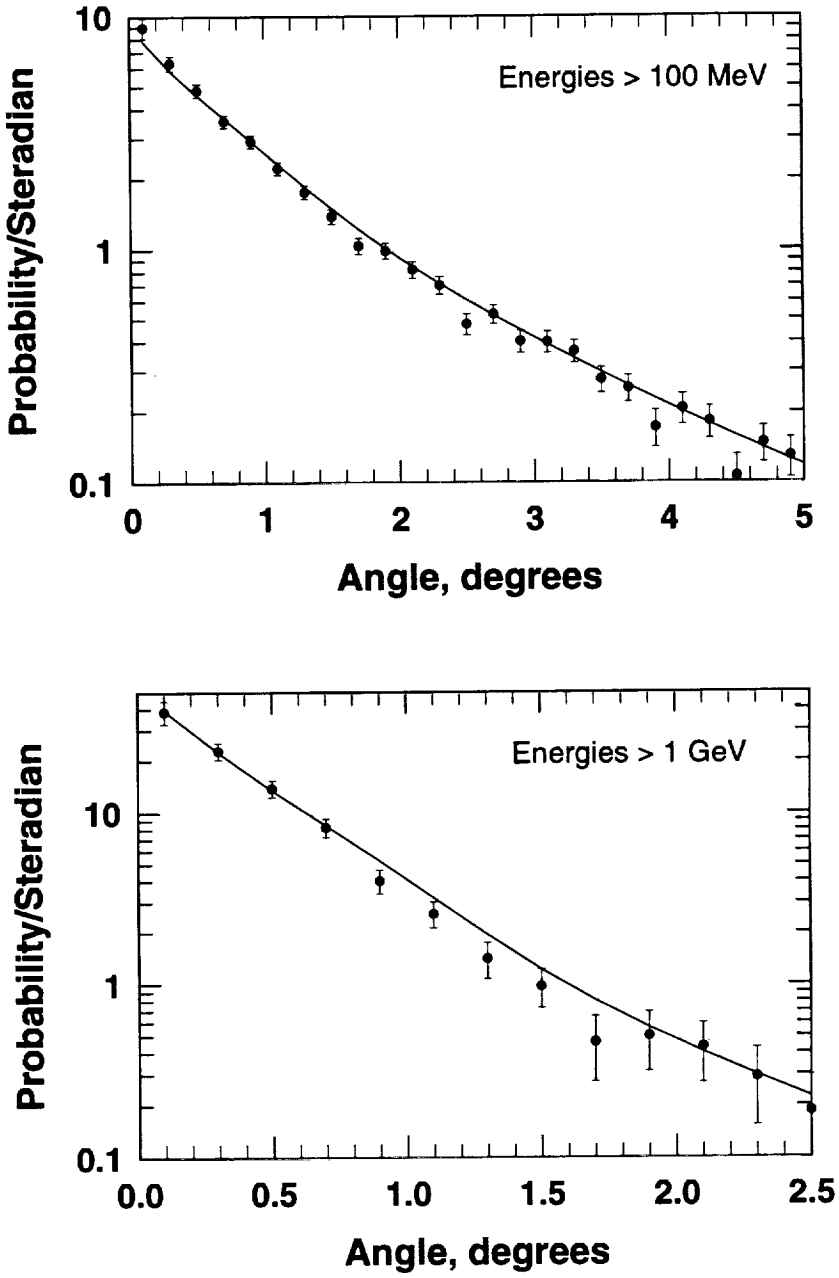

Fig. 5 – The EGRET point-spread function, measured in flight (see text) as a function of the angle from the instrument's Z-axis for the energy ranges indicated. The solid line is the functional fit to the pre-flight beam calibration measurements.

The behavior of the instrument off-axis was investigated using the same technique described in the previous sub-section. The off-axis models fit the off-axis data, although the statistics were worse than for the on-axis study. The models also fit the later viewing periods, again with worse statistics. Note that the models already take into account the known degradation in PSF as the source moves off-axis. Figure 6 shows the effect of the differing PSF as a function of inclination angle, using the bright, steady Crab, Geminga, and Vela pulsars as reference sources. If the on-axis PSF is used at wide angles (> 30°), the derived

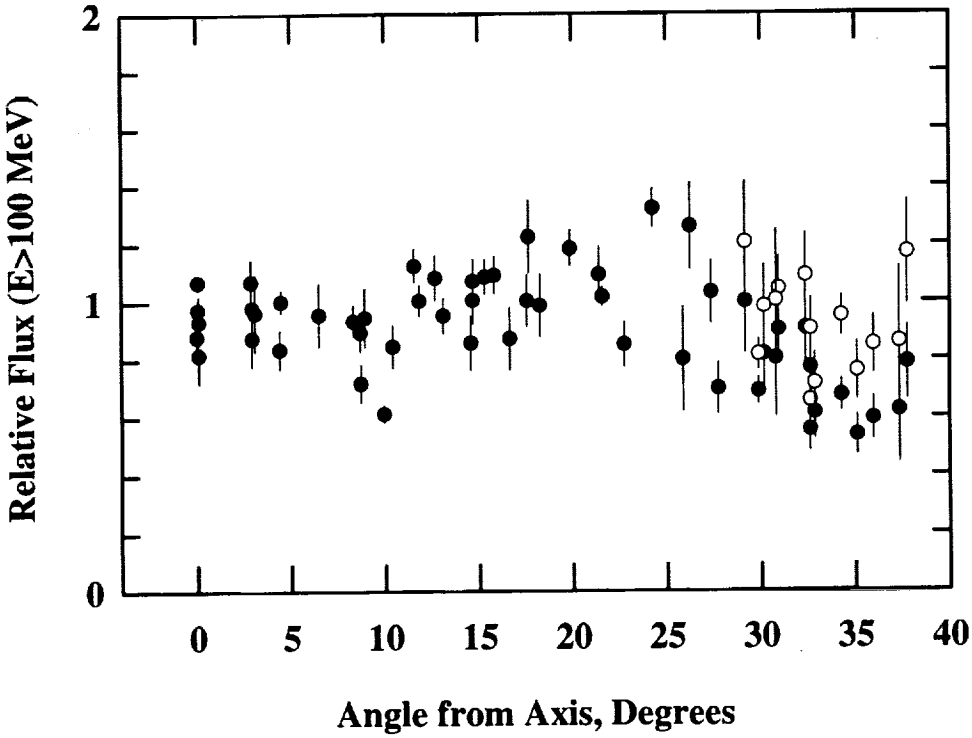

Fig. 6 – The dependence of flux measurements on the angle of the source from the instrument's Z-axis based on observations of the Crab, Geminga, and Vela pulsars. The flux values are shown relative to the average flux computed from maps summed over the first four cycles of *CGRO* observations, using all observations where the source was within 30° of the axis. Filled symbols: flux values calculated using low-inclination PSF; open symbols: flux values calculated using high-inclination PSF.

source flux is significantly lower than the flux seen on-axis. Using the correct wide-angle PSF produces flux values more consistent with those seen at small inclinations, although there is considerable scatter, and the average flux beyond 30° is 10 – 15% lower than the flux seen on-axis. In light of the scatter and the offset, we recommend that wide-angle flux values not be used in searches for small-scale source variability.

In conclusion, the SLAC calibration PSF values appear to match the in-flight data for all energies, all angles, and all observations, within the statistics of the pulsar observations used as a reference. The composite PSF used for broad energy bands must be constructed using the correct energy spectrum. In particular, for sources that exhibit a high energy cutoff such as pulsars, the composite PSF must be constructed with spectral features in the model. If the input trial spectrum used to construct the PSF differs significantly from the output spectrum, one or more iterations in the analysis may be required. No significant time variability has been found in the PSF shape or extent. Finally, the wide-angle PSF is broader than the PSF close to the instrument axis. For analysis at wide angles, the proper calibration file entries must be used. This implies that sources near axis, angles less than 30°, should be analyzed separately from sources at wide angles.

5. Energy Calibration Studies

Before launch the PMT high voltages were adjusted to make the response over the TASC surface as uniform as possible. In-flight measurements of the TASC calorimeter response are used to determine time-dependent calibration of photon-energy measurements. The only useful energy-calibration standards are gamma-ray lines that can be observed in the low-energy PHAs. The two best lines are produced by materials in the spacecraft structure: radioactive ^{40}K (1.46 MeV) (present in the spark chamber frames) and neutron capture by iron (7.6 MeV) in the spacecraft. These lines can be seen in the spectra that are continuously accumulated. Figure 7 shows a recent one-day accumulated spectrum used to check the energy calibration utilizing these two background lines. Note that in the second panel of this figure, the shoulder at channel 282 is the important feature and not the peak at channel 500. The peak at channel 500 is a hardware artifact that arises the high energy processor's analysis of events that trigger the spark chamber. The ability to calibrate individual parts of the system is limited by several factors. The high-energy PHAs cannot detect the calibration lines at all; it is necessary to assume that their behavior scales with the same corrections as the low energy processors. Individual PMTs cannot be examined in isolation; if seven of the eight PMTs in a group are turned off, the apparent energy of the lines will fall below the PHA threshold. Calibration of the two PMT groups can be compared only by turning

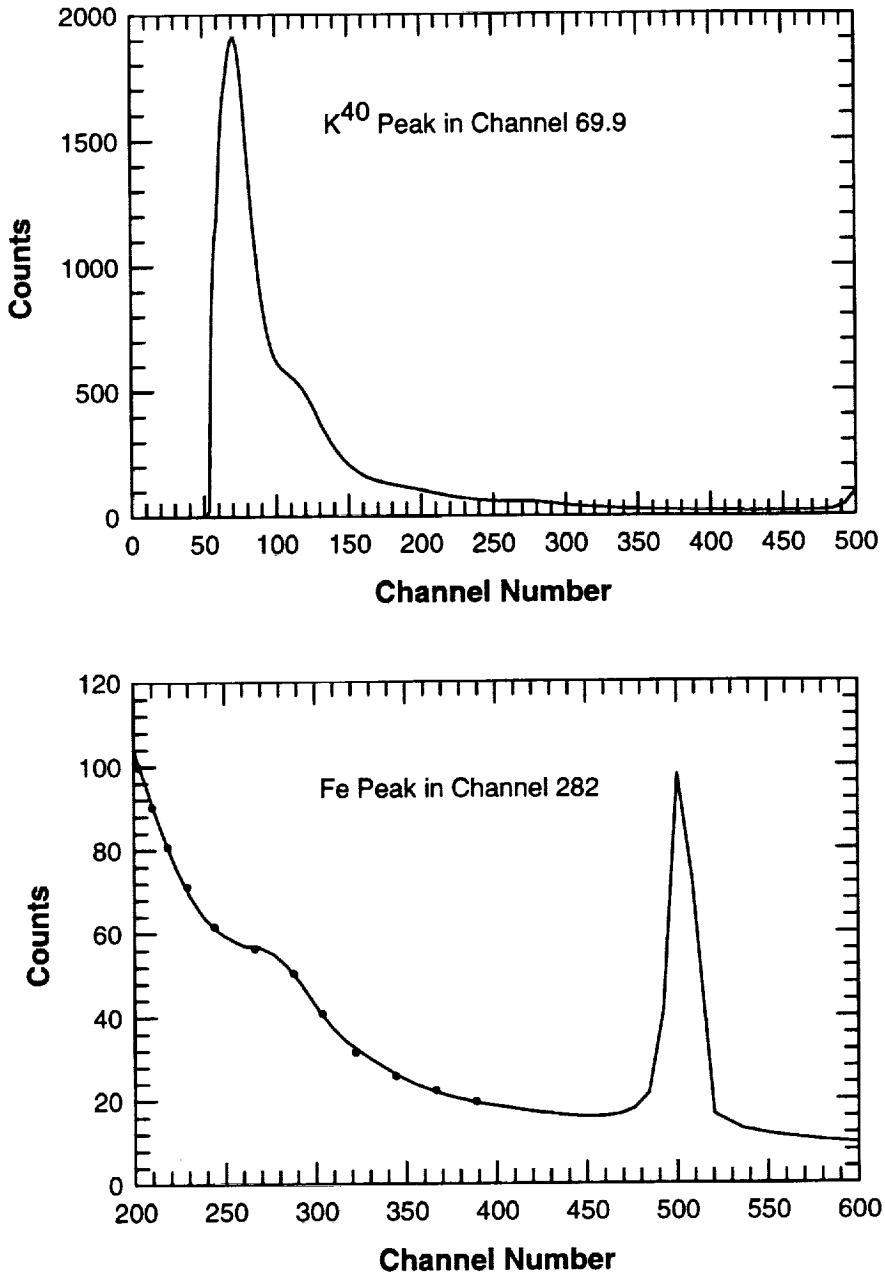

Fig. 7 – A one-day average of the spectra accumulated by the Total Energy Absorption Shower Counter (TASC) every 32.8s. The two line signatures are used to determine energy calibration of the TASC. The dots show a modeled fit to the region from channels 200 to 300.

The fit is based on a Gaussian plus two power laws. The peak of the Gaussian at this time is at channel 282.1. Note that the peak located near channel 500 is an artifact as described in the text.

off the two halves of the TASC electronics that control the groups; this has been done only once as a test.

The energy resolution has degraded with time, apparently through unequal drifts in individual PMTs. Although this is significant for the low-energy (solar and burst) modes, the TASC energy resolution is a fairly minor component of the total detector resolution for triggered events. Shortly after the *CGRO* launch on 1991 April 5, it was evident that the overall TASC gain had decreased by about 14% from the value measured before launch. Furthermore, the ratio of the gains in the two low-energy PHAs changed by 5.5%. Finally, the average gain was decreasing at a rate of 0.14% per day. The initial shifts might have been caused by disturbances to the PMT optical couplings at launch. No convincing explanation has been advanced for the continuing drift. On 1991 July 17 (See Table 1), the high voltages of all the PMTs were adjusted to compensate for these effects. The voltage adjustments were based on measurements of the nonlinear gain characteristics of the individual tubes made before their installation in EGRET. The gain drift has continued ever since, but the rate has decreased to a stable value of 0.024% per day. Further PMT voltage increases were made on 1993 February 2 and 1995 April 25, each time enough to boost the gain by 20%.

It is necessary to correct the raw measured photon energies for the gain drift. When they are placed in the EGRET database, the true energies of the individual photons detected by the spark chamber are estimated by an algorithm that contains a model of the PMT drift as a function of time. The EGRET spark chamber event data available from the *CGRO* Science Support Center (SSC) are corrected for the gain drift, but the TASC solar and burst spectra are not, since it is the bin boundaries that are affected. The EGRET low-energy analysis software makes the adjustment at the time of analysis.

5.1. High-Energy Events of Lower Quality

EGRET gamma-ray events are divided into three classes, A, B, and C. Class A contains the best quality of energy analysis where both the electron and positron enter the TASC, and the total energy deposited exceeds the threshold of 20 MeV required for the high energy PHA. In Class B, only one of the particles enters the TASC (based on the spark chamber image), and the second particle either exits the side of the spark chamber or stops in material above the TASC. includes events where both particles enter the TASC but the 20 MeV threshold

is not triggered. Classes B and C rely on multiple scattering measurements to complete the energy analysis; however, scattering measurements have large uncertainties and are effective only for particle energies below about 150 MeV. For this reason, Class B events are of distinctly poorer energy resolution than Class A events of the same energy. Because Class C events are low energy, the scattering estimates are reliable, making Class C of better quality than Class B. At energies < 70 MeV, virtually all of the events are of Class C.

For Class B events, the energy estimation software has a design flaw that causes a pile-up of events from energies above 3 GeV to be distributed just below 3 GeV. Usually, Class B and Class C events are included in the analysis despite their lower quality since limited statistics dominate the uncertainty in the spectral fitting. For almost all spectra the so-called "3 GeV pile-up" effect is negligible, especially when the standard 2 to 4 GeV energy bin is used in which case the effect nearly washes out. However, for studies of the diffuse galactic emission (and possibly long accumulations for Vela pulsar, the most intense source) where large numbers of photons allow narrow energy bands even at high energies, the artifact feature can appear to be a 3 GeV emission line. Because the software flaw affects only studies of the galactic diffuse emission, no attempt is planned to reprocess the seven-year database with a corrected energy algorithm. Instead, correction factors for the energy analysis artifact, as determined by Hunter et al. (1997) (See especially Figure 4 of that paper.) for the galactic diffuse emission are given in Table 2. The values in this table should be applied to the measured intensity only when Class B events are included.

6. EGRET Viewing Modes

The primary EGRET operating modes, described in Thompson et al. (1993), are: (a) events accepted over the full opening angle of the instrument, with an added coincidence requirement that each event trigger a ~ 6 MeV discriminator in the TASC-energy-measurement system; (b) the same full acceptance angle, without the energy deposition requirement. Table 3 summarizes the timeline history of EGRET's pointing and operating modes through Cycle 7. The full field of view mode that was used almost entirely through Cycle 4 is designated by the letter "W" in the mode column. The TASC coincidence condition is also given, and it is almost always required as part of the trigger.

As mentioned in Section 2, the coincidence requirements for the two coincidence planes are set to select the unocculted directions. Anticipating that some other operating modes might be used, the original calibration of EGRET was carried out using the minimum trigger requirement, equivalent to mode (b). However, each event recorded during calibration contains information about the energy deposited in various segments of the instrument, so

Table 2: Correction Factors for the Anomalous High Energy Feature

Energy Range (MeV)		Spectral Index		
		1.80	2.20	2.60
Low	High	Factors		
100	300	1.00	1.00	1.00
300	500	1.00	1.00	1.00
500	1,000	1.00	1.00	1.00
1,000	2,000	0.99	0.99	0.99
2,000	4,000	0.96	0.95	0.95
4,000	10,000	1.09	1.11	1.15
> 100		1.00	1.00	1.00
> 1,000		1.01	1.00	0.99
> 4,000		1.09	1.11	1.12
>10,000		1.00	1.00	1.00

that the calibration data can be re-analyzed for different operating conditions. Beginning in Cycle 4 of the mission, some new modes of operation were indeed found to be necessary.

On 1994 October 28, one of the 32 photo-multiplier tubes in the EGRET coincidence system failed, and new calibration files were constructed by re-analyzing the calibration data, excluding those events whose trigger depended on the failed tube. Because the coincidence system had 16 photo-multiplier tubes in each layer, the loss of one tube represents a net loss of sensitivity of only about 6%. All calibration files used after this time take into account this loss. The sensitivity analysis is complicated significantly by the loss of symmetry resulting from this failure.

In order to reduce the number of triggers and thereby prolong the gas lifetime, it was decided to operate EGRET more often in a "narrow field of view mode" after the completion of the first four cycles of the *CGRO* mission. Therefore, in Cycle 4 EGRET was reconfigured for some test observations into a narrower field of view. These periods are shown in Table 3 with the mode designation "N". During Cycles 5 and beyond, all observations are carried out in reduced-FOV modes. In almost all cases, only the 15 pairs of vertically aligned scintillator tiles (the "vertical" or axial mode) have been used to trigger the instrument (16

original pairs minus the one lost because of the PMT failure described above). The narrow field mode has a reduction from a 30° radius to 19° radius, defined at a level where the exposure is roughly 10% of the axial exposure. Thus the field-of-view is reduced in width by $\sim 35\%$, and the trigger rate is about 1/4 that of the wide-field mode. The on-axis instrument sensitivity is approximately 80% of the wide-field configuration for energies below 500 MeV due to energy dependent scattering of the electron and positron pair. At lower energies, it is more probable that both charged particles scatter so that neither hits the lower, vertically adjacent, scintillator tile. At the highest energies ($E \geq 1000$ MeV) the decrease of the on-axis sensitivity is almost negligible.

In 1996 September, still another mode was used for EGRET. In this case, the field of view was open in one dimension while being restricted in the orthogonal dimension (Strip- or Fan-Mode, viewing period 530.0). The spacecraft was then oriented so that the long axis of the exposure pattern covered multiple targets of interest. Because this mode places additional constraints on spacecraft operation, it is not expected to be used frequently.

Figure 8 shows the effective area as a function of angle for the different modes and for two energy regimes, $E > 100$ MeV and $E > 1000$ MeV.

7. Background – Earth-Limb Albedo

The largest source of non-celestial gamma-ray background events is from atmospheric albedo. The EGRET trigger is dynamically adjusted during flight to minimize triggering from these atmospheric gamma rays. However, due to the large number of these events, EGRET still triggers on a small fraction of albedo gamma rays. The angular distributions of measured gamma-ray zenith angles are depicted in Figure 9 for two energy selections. The large peak to the right of each distribution is due to albedo gamma rays for the worst case spacecraft orientation (pointing roughly perpendicular to the orbit plane). These events are removed from further data analysis by imposing an energy-dependent zenith angle cut θ_{cut}, given by the vertical lines in Figure 9.

$$\theta_{cut} = \min[105°, f \times 5.85° \times (E/100\,\mathrm{MeV})^{-0.534}] \tag{6}$$

where E is the lower energy bound of the energy interval of interest. The factor f is normally selected to be 2.5, but for high-latitude diffuse studies a more severe value of 4.0 was used (Sreekumar et al. 1998). The dashed-line cut ($f = 2.5$) is quite satisfactory for point-source analysis, or for analysis of galactic diffuse emission. The dotted line in Figure 9 ($f = 4.0$) indicates the level of the more restrictive cut, which has been found necessary only for

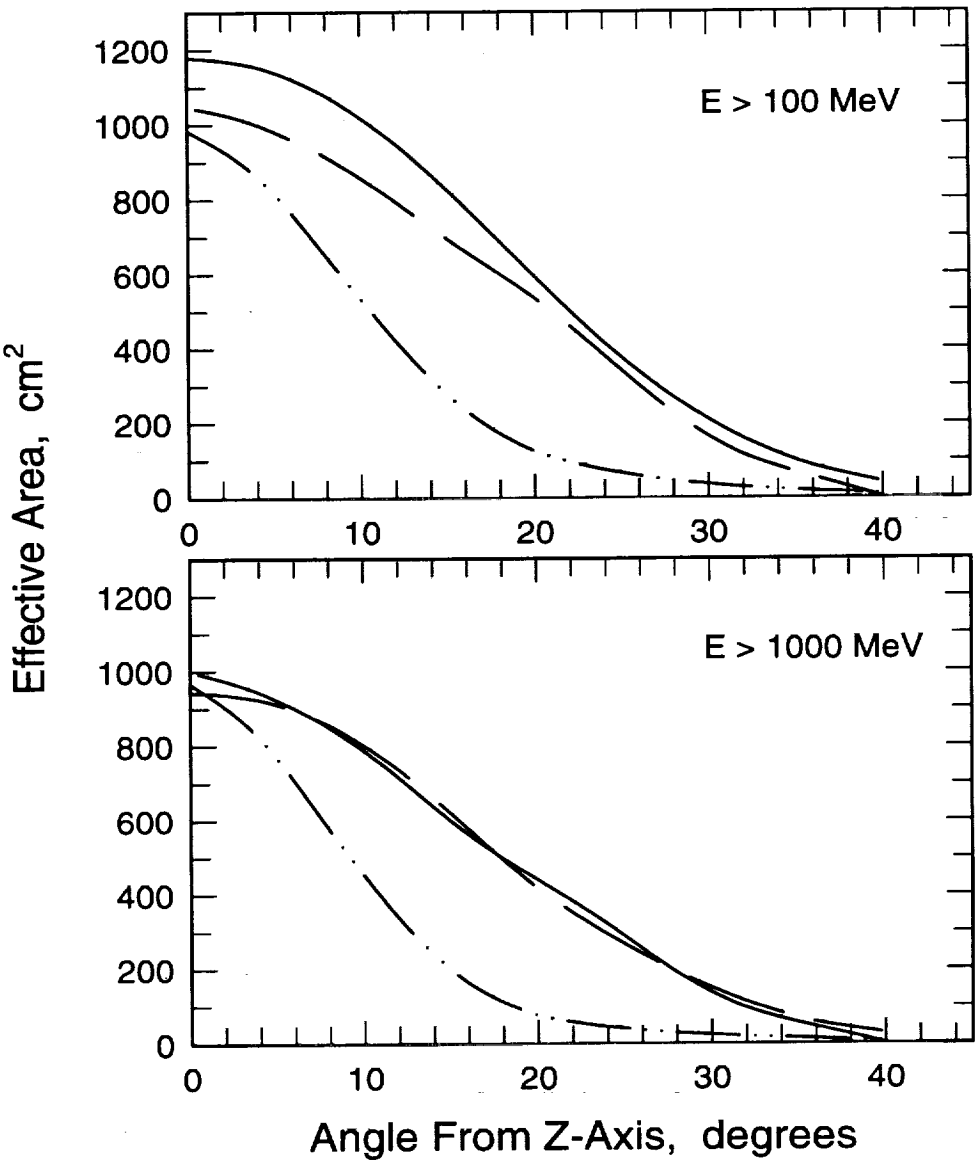

Fig. 8 – The EGRET effective area as a function of the incidence angle for the three different telescope modes. The solid curves are for the wide-angle mode, the dashed curves are for the strip mode for sources along the long axis, and the dash-dot curves are for the narrow angle mode. Two energy regimes are shown as noted.

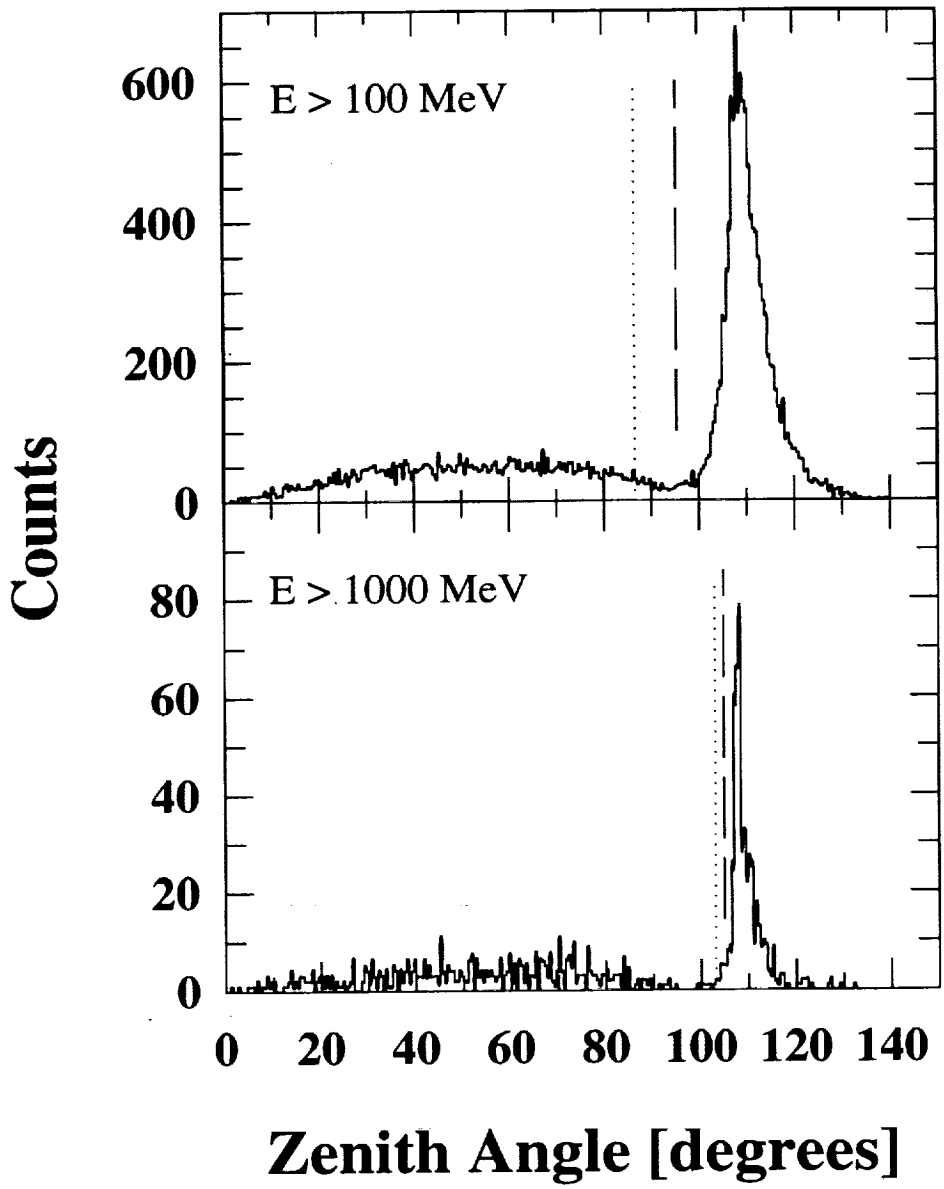

Fig. 9 – EGRET photon counts, binned by the Earth zenith angle. Events that are due to the atmosphere albedo are concentrated in the peaks to the right of histogram. The cuts used for the analysis of point sources and galactic diffuse emission are shown by the dashed lines. A more severe cut, shown by the dotted lines, was used for the extra-galactic diffuse emission analysis.

analysis of the lower-intensity high-latitude emission.

8. Summary

EGRET was designed for a two-year mission but its lifetime has been extended to over seven years, and it is still operational. This added lifetime arises in part by extending the consumable gas resource to levels where the instrument sensitivity has decreased significantly. Also, some hardware failures have occurred that influenced the sensitivity. The method used to determine the in-flight calibration of EGRET's effective area as a function of time and energy has been presented. The results of the analysis are based primarily on observations of the diffuse emission together with the assumption that the instrument performance early in the mission and at periods after the first three gas fills were similar to when the instrument was calibrated at SLAC. The point-spread-function was studied in detail as a function of arrival angle and energy using pulsar data with the conclusion that there has been no significant change since launch.

The calibration study has also identified analysis issues that have been discussed here including (a) the importance in using an iterated spectral fit to insure that the PSF is properly constructed when wide energy intervals are used, (b) using the wide-angle PSF when sources are more than 30° from axis, and (c) correcting for the "3 GeV pile-up" effect for energies above 1 GeV when Class B energy events are included and high statistics ($\sim$ 10% uncertainty, or better) are available.

The extended lifetime of the EGRET instrument has made it necessary to apply corrections to the pre-flight calibration parameters that have been described here. For some observations, these corrections are quite large. On the other hand, the scientific payoff of the mission extension has been very significant in terms of the additional detections of unidentified sources, pulsar timing and long-term studies, new blazar detections and multi-wavelength campaigns to monitor their intensity and spectral variations, and in observing the galactic and extra-galactic diffuse emission. All of these observations have important scientific implications. It is anticipated that EGRET will continue to operate throughout *CGRO* Cycle 8 with a lowered, but correctable, instrument sensitivity, and that continual monitoring will be needed to implement correction factors for the instrument's remaining life.

All EGRET data products, data product updates, and analysis software developed by the Instrument Team have been, and will continue to be, delivered to the *CGRO* Science Support Center.

Acknowledgments

The EGRET Team gratefully acknowledges support from the following: Bundesministerium für Bildung, Wissenschaft, Forschung und Technologie (BMBF), Grant 50 QV 9095 (MPE); NASA Cooperative Agreement NCC 5-93 (HSC); NASA Cooperative Agreement NCC 5-95 (SU); and NASA Contract NAS5-96051 (NGC). This work was also supported by the Deutsche Forschungsgemeinschaft (Sonderforschungsbereich 328).

REFERENCES

Bertsch, D. L., Dame, T. M., Fichtel, C. E., Hunter, S. D., Sreekumar, P., Stacy, J. G., & Thaddeus, P. 1993, ApJ, 416, 587

Bignami, G. F., et al. 1975, Space Sci. Inst., 1, 245

Derdeyn, S. M., Ehrmann, C. H., Fichtel, C. E., Kniffen, D. A., and Ross, R. W. 1972, NIM, 98, 557

Fichtel, C. E., 1996 A&AS, 120, 23

Fierro, J. M., Michelson, P. F., Nolan, P. L., & Thompson, D. J. 1998, ApJ, 494, 734

Hartman, R.C., et al. 1998, ApJ, in press

Hughes, E. B., et al. 1980, IEEE Trans. Nucl. Sci., NS-27, 364

Hughes, E. B., et al. 1986, IEEE Trans. Nucl. Sci., NS-33, 728

Hunter, S. D., et al. 1997, ApJ, 481, 205

Kanbach, G., et al. 1988, Sp. Sci. Rev., 49, 69

Kanbach, G., et al. 1989, in Proc. Gamma Ray Observatory Sci. Workshop, ed. W. N. Johnson (Greenbelt, MD: NASA), 2-1

Mattox, J. R., et al. 1996, ApJ, 461, 396

McLaughlin, M. A., Mattox, J. R., Cordes, J. M., and Thompson, D. J. 1996, ApJ, 473, 763

Ramanamurthy, P.V., et al. 1995, ApJ, 481, 205

Simpson, G., & Mayer-Hasselwander, H. A. 1985, A&A, 162, 340

Strong, A.W. et al. 1987, A&A Supp, 67, 283

Sreekumar, P., et al. 1998, ApJ, 494, 523

Thompson, D. J., et al. 1993, ApJS, 86, 629

Thompson, D. J., et al. 1995, ApJS, 101, 259

Willis, T. D. 1996, Ph.D. thesis, Stanford Univ.

This preprint was prepared with the AAS LaTeX macros v4.0.

Table 3. EGRET Timeline Summary

View Per.	Start Date	Start Time hh:mm	End Date	End Time hh:mm	Inst. Mode†	Z-Axis R.A. Deg.	Z-Axis Dec. Deg.	Target Region
0002	04/22/91	21:09	04/28/91	15:12	W,T	86.76	22.09	Crab Pulsar
0003	04/28/91	16:02	05/01/91	16:37	W,T	89.80	15.25	Crab Pulsar
0004	05/01/91	17:19	05/04/91	16:16	W,T	89.77	15.24	Crab Pulsar
0005	05/04/91	16:50	05/07/91	15:53	W,T	83.52	22.02	Crab Pulsar
0006	05/07/91	16:32	05/10/91	19:40	W,T	162.44	57.26	GAL 150+53
0007	05/10/91	20:15	05/16/91	16:39	W,T	135.19	-45.11	Vela Pulsar
0010	05/16/91	17:19	05/30/91	18:51	W,T	88.07	17.14	Crab Pulsar
0020	05/30/91	20:01	06/08/91	00:08	W,T	301.39	36.58	CYG X-1
0021	06/08/91	01:24	06/15/91	18:44	W,T	87.83	12.47	Sun
0030	06/15/91	19:38	06/28/91	19:30	W,T	191.54	2.62	SN 1991T
0040	06/28/91	20:14	07/12/91	17:56	W,T	179.84	41.52	NGC 4151
0050	07/12/91	18:48	07/26/91	19:25	W,T	270.39	-30.96	Gal Center
0060	07/26/91	20:25	08/08/91	15:36	W,T	91.28	-67.96	SN 1987A
0071	08/08/91	17:00	08/15/91	17:29	W,T	310.05	28.06	Cygnus X-3
0072	08/15/91	18:23	08/22/91	14:05	W,T	291.98	-13.27	GAL 025-14
0080	08/22/91	15:01	09/05/91	14:01	W,T	124.96	-46.35	Vela Pulsar
0091	09/05/91	15:03	09/12/91	13:24	W,T	8.34	-32.31	GAL 339-84
0092	09/12/91	14:34	09/19/91	13:29	W,T	251.27	36.89	HER X-1
0100	09/19/91	14:36	10/03/91	13:11	W,T	30.91	-60.66	GAL 288-54
0110	10/03/91	14:10	10/09/91	12:00	W,T	189.02	1.06	3C 273
	10/09/91	12:00	10/10/91	12:00	W,O			
	10/10/91	12:00	10/11/91	12:00	W,T			
	10/11/91	12:00	10/12/91	12:00	W,O			
	10/12/91	12:00	10/13/91	12:00	W,T			
	10/13/91	12:00	10/14/91	12:00	W,O			
	10/14/91	12:00	10/15/91	12:00	W,T			
	10/15/91	12:00	10/16/91	12:00	W,O			
	10/16/91	12:00	10/17/91	13:57	W,T			
0120	10/17/91	15:15	10/31/91	14:55	W,T	202.29	-40.09	CEN A
0131	10/31/91	15:42	11/07/91	14:34	W,T	291.98	-13.27	GAL 025-14
0132	11/07/91	15:30	11/14/91	15:45	W,T	8.34	-32.31	GAL 339-84
0140	11/14/91	16:50	11/19/91	12:00	W,T	156.83	-58.51	Eta Car
	11/19/91	12:00	11/20/91	12:01	W,O			
	11/20/91	12:01	11/21/91	12:00	W,T			

Table 3—Continued

View Per.	Start Date	Start Time hh:mm	End Date	End Time hh:mm	Inst. Mode†	Z-Axis R.A. Deg.	Z-Axis Dec. Deg.	Target Region
	11/21/91	12:00	11/22/91	12:00	W,O			
	11/22/91	12:00	11/23/91	11:59	W,T			
	11/23/91	11:59	11/24/91	12:00	W,O			
	11/24/91	12:00	11/28/91	11:30	W,T			
0150	11/28/91	12:50	12/12/91	16:42	W,T	52.00	40.24	NGC 1275
0160	12/12/91	18:00	12/27/91	16:02	W,T	248.35	-17.20	GAL 000+20
0170	12/27/91	17:07	01/10/92	16:15	W,T	83.48	-72.26	SN 1987A
0180	01/10/92	18:12	01/23/92	13:42	W,T	154.60	72.04	M 82
0190	01/23/92	15:08	02/06/92	15:15	W,T	331.40	-1.93	GAL 058-43
0200	02/06/92	16:45	02/18/92	06:00	W,T	285.28	6.37	GAL 040+01
	02/18/92	06:00	02/20/92	06:00	W,O			
	02/20/92	06:00	02/20/92	15:03	W,T			
0210	02/20/92	16:05	03/05/92	15:49	W,T	39.09	-1.24	NGC 1068
0220	03/05/92	16:45	03/19/92	13:19	W,T	216.00	70.74	MRK 279
0230	03/19/92	14:15	03/21/92	06:00	W,T	227.43	-54.62	CIR X-1
	03/21/92	06:00	03/22/92	06:00	W,O			
	03/22/92	06:00	03/23/92	06:00	W,T			
	03/23/92	06:00	03/24/92	06:00	W,O			
	03/24/92	06:00	03/25/92	06:00	W,T			
	03/25/92	06:00	03/26/92	06:00	W,O			
	03/26/92	06:00	03/27/92	06:00	W,T			
	03/27/92	06:00	03/28/92	06:00	W,O			
	03/28/92	06:00	04/02/92	12:49	W,T			
0240	04/02/92	14:07	04/09/92	13:02	W,T	223.34	11.03	GAL 010+57
0245	04/09/92	13:26	04/16/92	12:29	W,T	223.34	11.03	GAL 010+57
0250	04/16/92	13:17	04/23/92	12:27	W,T	229.85	4.47	GAL 007+48
0260	04/23/92	13:29	04/28/92	12:44	W,T	1.59	20.20	MRK 335
0270	04/28/92	13:41	05/07/92	14:08	W,T	241.11	-49.05	4U 1543-47
0280	05/07/92	14:47	05/14/92	14:04	W,T	1.59	20.20	MRK 335
0290	05/14/92	14:48	06/04/92	13:44	W,T	68.97	-25.09	GAL 224-40
0300	06/04/92	14:50	06/11/92	14:04	W,T	149.50	-14.73	NGC 2992
0310	06/11/92	16:25	06/25/92	13:17	W,T	88.87	49.44	MCG +8-11-11
0320	06/25/92	14:20	07/02/92	13:57	W,T	171.17	-36.81	NGC 3783
0330	07/02/92	15:06	07/16/92	15:34	W,T	149.50	-14.73	NGC 2992

Table 3—Continued

View Per.	Start Date	Start Time hh:mm	End Date	End Time hh:mm	Inst. Mode†	Z-Axis R.A. Deg.	Z-Axis Dec. Deg.	Target Region
0340	07/16/92	17:25	08/06/92	14:38	W,T	345.77	57.49	CAS A
0350	08/06/92	16:35	08/11/92	00:54	W,T	287.12	-61.21	GAL 335-26
0360	08/11/92	02:00	08/12/92	18:22	W,T	68.98	30.42	GAL 170-10
0365	08/12/92	19:20	08/20/92	15:28	W,T	69.39	32.90	GAL 170-10
0370	08/20/92	16:02	08/27/92	16:49	W,T	358.75	18.82	MRK 335
0380	08/27/92	18:45	09/01/92	04:37	W,T	287.12	-61.21	ESO 141-55
0390	09/01/92	06:18	09/17/92	15:17	W,T	68.87	33.82	GRO J0424+32
0400	09/17/92	16:15	10/08/92	13:48	W,T	140.88	30.40	MCG +5-23-16
0410	10/08/92	15:11	10/15/92	16:18	W,T	112.43	-12.05	GAL 228+03
0420	10/15/92	17:10	10/29/92	13:31	W,T	319.72	-41.67	PKS2155-304
0430	10/29/92	15:30	11/03/92	13:07	W,T	307.83	-13.95	MRK 509
0440	11/03/92	15:10	11/17/92	14:57	W,T	112.43	-12.05	GAL 228+03
2010	11/17/92	17:10	11/24/92	16:23	W,T	253.15	42.26	HER X-1
2020	11/24/92	17:50	12/01/92	15:29	W,T	251.55	45.40	HER X-1
2030	12/01/92	17:04	12/22/92	13:58	W,T	306.59	39.34	CYGNUS
2040	12/22/92	14:44	12/29/92	15:32	W,T	188.99	-0.74	3C 273
2050	12/29/92	16:12	01/05/93	14:22	W,T	188.84	-1.03	3C 273
2060	01/05/93	15:01	01/12/93	14:54	W,T	188.99	-0.74	3C 273
2070	01/12/93	15:42	02/02/93	14:33	W,T	203.86	-30.41	IC 4329A
2080	02/02/93	15:10	02/09/93	16:12	W,T	198.47	-41.93	NGC 4507
2090	02/09/93	18:15	02/22/93	16:06	W,T	305.69	-40.81	2CG 010-31
2100	02/22/93	17:15	02/25/93	14:15	W,T	257.65	-29.10	Gal Center
2110	02/25/93	17:03	03/09/93	15:08	W,T	18.38	58.05	GAL 123-05
2120	03/09/93	15:56	03/23/93	16:40	W,T	297.88	50.15	WR 140
2130	03/23/93	18:40	03/26/93	18:16	W,T	80.30	22.29	CRAB Pulsar
	03/26/93	18:16	03/29/93	13:02	W,O			
2140	03/29/93	14:57	04/01/93	15:50	W,T	257.65	-29.10	Gal 356+06
2150	04/01/93	16:51	04/06/93	19:27	W,T	203.26	-39.28	CEN A
2160	04/06/93	20:50	04/12/93	12:43	W,T	143.66	71.46	SN 1993J
2170	04/12/93	13:50	04/20/93	14:18	W,T	203.26	-39.28	CEN A
2180	04/20/93	15:23	05/05/93	13:55	W,T	180.75	43.09	NGC 4151
2190	05/05/93	16:00	05/08/93	13:24	W,T	245.35	-27.22	GAL 350+16
2200	05/08/93	14:55	05/13/93	15:27	W,T	24.11	-72.07	SMC
2210	05/13/93	16:29	05/21/93	11:15	W,T	85.21	19.46	CRAB Pulsar

Table 3—Continued

View Per.	Start Date	Start Time hh:mm	End Date	End Time hh:mm	Inst. Mode†	Z-Axis R.A. Deg.	Z-Axis Dec. Deg.	Target Region
	05/21/93	11:15	05/24/93	15:17	W,O			
2220	05/24/93	17:10	05/31/93	13:33	W,T	178.02	42.25	NGC 4151
2230	05/31/93	14:35	06/03/93	14:41	W,T	265.98	-29.72	Gal Center
2240	06/03/93	16:30	06/19/93	13:03	W,T	24.11	-72.07	SMC
2260	06/19/93	14:35	06/29/93	14:04	W,T	258.44	-30.35	GAL 335+05
2270	06/29/93	15:00	07/13/93	13:27	W,T	143.64	65.00	SN 1993J
2280	07/13/93	14:07	07/27/93	12:43	W,T	145.33	63.18	SN 1993J
2300	07/27/93	14:03	07/30/93	13:46	W,T	143.03	-54.64	Vela Pulsar
2305	07/30/93	14:23	08/03/93	13:45	W,T	149.86	-53.17	Vela Pulsar
2310	08/03/93	20:39	08/10/93	13:56	W,T	289.94	-15.33	NGC 6814
2290	08/10/93	14:52	08/11/93	16:41	W,T	264.60	-22.06	GAL 005+05
2293	08/11/93	17:33	08/12/93	14:01	W,T	-1.00	-1.00	Perseid shower
2295	08/12/93	14:52	08/17/93	14:16	W,T	264.60	-22.06	GAL 005+05
3010	08/17/93	23:04	08/24/93	13:53	W,T	128.92	-45.18	Vela Pulsar
2320	08/24/93	14:52	09/07/93	14:09	W,T	258.02	-39.35	GAL 348+00
3020	09/07/93	19:57	09/09/93	13:22	W,T	307.63	52.63	N CYG 1992
3023	09/09/93	14:19	09/21/93	14:23	W,T	258.63	-22.70	GX 1+4
3030	09/21/93	15:22	09/22/93	14:44	W,T	157.58	-42.88	GRS 1009-45
3032	09/22/93	16:06	10/01/93	15:00	W,T	307.63	52.63	N CYG 1992
3034	10/01/93	16:00	10/04/93	14:00	W,T	270.79	37.87	reboost att.
3037	10/17/93	22:34	10/19/93	15:11	W,T	307.63	52.63	N CYG 1992
3040	10/19/93	16:19	10/25/93	14:31	W,T	183.29	5.68	VIRGO 278+67
3050	10/25/93	15:40	11/02/93	14:56	W,T	181.58	2.06	VIRGO 278+63
3060	11/02/93	15:32	11/09/93	13:09	W,T	180.01	-1.62	VIRGO 278+59
3070	11/09/93	13:47	11/16/93	14:25	W,T	181.19	9.53	VIRGO 269+69
3080	11/16/93	15:11	11/19/93	10:01	W,T	187.61	12.59	VIRGO 283+75
3086	11/23/93	22:10	12/01/93	14:42	W,T	187.61	12.59	VIRGO 284+75
3100	12/01/93	15:42	12/13/93	15:14	W,T	98.48	17.77	Geminga Psr.
3110	12/13/93	16:10	12/15/93	11:04	W,T	187.69	12.41	VIRGO 283+75
3116	12/17/93	23:07	12/20/93	13:32	W,T	187.69	12.41	VIRGO 283+75
3120	12/20/93	14:15	12/27/93	15:26	W,T	185.52	9.12	VIRGO 283+71
3130	12/27/93	16:06	01/03/94	15:34	W,T	190.10	16.12	VIRGO 289+79
3140	01/03/94	16:32	01/16/94	15:17	W,T	195.69	-63.83	GAL 304-01
3150	01/16/94	15:55	01/23/94	15:30	W,T	195.69	-63.83	GAL 304-01

Table 3—Continued

View Per.	Start Date	Start Time hh:mm	End Date	End Time hh:mm	Inst. Mode†	Z-Axis R.A. Deg.	Z-Axis Dec. Deg.	Target Region
3160	01/23/94	16:16	02/01/94	14:32	W,T	201.37	-43.02	CEN A
3181	02/01/94	15:30	02/08/94	14:46	W,T	301.26	30.92	Cyg-X1
3211	02/08/94	15:39	02/15/94	14:47	W,T	84.73	26.32	Gal Anticenter
3215	02/15/94	15:22	02/17/94	15:16	W,T	84.73	26.32	Gal Anticenter
3170	02/17/94	16:00	03/01/94	13:32	W,T	37.41	10.61	3C 120
3190	03/01/94	14:30	03/08/94	15:28	W,T	110.48	71.34	QSO 0716+714
3200	03/08/94	16:40	03/15/94	14:02	W,T	345.81	8.87	GAL 083-45
3195	03/15/94	15:15	03/22/94	14:04	W,T	105.20	68.99	QSO 0716+714
3230	03/22/94	15:20	04/05/94	14:24	W,T	276.44	-37.11	GAL 357-11
3220	04/05/94	15:35	04/19/94	14:49	W,T	157.07	31.09	MRK 4216+714
3240	04/19/94	15:50	04/26/94	13:16	W,T	269.39	-13.15	GAL 016+05
3250	04/26/94	14:22	05/10/94	14:59	W,T	49.07	46.94	GAL 147-09
3260	05/10/94	15:57	05/17/94	13:39	W,T	156.69	31.65	NGC 3227
3270	05/17/94	14:55	05/24/94	13:44	W,T	348.06	5.44	GAL 083-45
3280	05/24/94	14:33	05/31/94	13:55	W,T	298.76	28.07	PSR 1951+32
3290	05/31/94	14:55	06/07/94	14:01	W,T	69.26	-47.25	GAL 253-42
3310	06/07/94	15:15	06/10/94	13:33	W,T	298.76	28.07	PSR 1951+32
3300	06/10/94	14:10	06/14/94	14:02	W,T	275.93	-13.26	GAL 018+00
3315	06/14/94	14:48	06/18/94	14:31	W,T	298.76	28.07	PSR 1951+32
3320	06/18/94	15:18	07/05/94	14:28	W,T	275.93	-13.26	GAL 010+00
3330	07/05/94	14:49	07/12/94	14:31	W,T	298.76	28.07	PSR 1951+32
3350	07/12/94	15:26	07/18/94	13:43	W,T	69.26	-47.25	GAL 253-42
3340	07/18/94	15:07	07/25/94	13:47	W,T	279.49	-25.06	GAL 009-08
3355	07/25/94	14:45	08/01/94	13:15	W,T	69.26	-47.25	GAL 253-42
3360	08/01/94	14:58	08/04/94	13:22	W,T	349.67	9.72	GAL 088-47
3365	08/04/94	14:25	08/09/94	21:12	W,T	249.14	-43.04	GRO J1655-40
3370	08/09/94	22:22	08/29/94	14:15	W,T	87.70	0.98	PKS 0528+134
3380	08/29/94	15:30	08/31/94	14:27	W,T	253.50	-39.85	CYG X3
3385	08/31/94	15:24	09/20/94	13:47	W,T	128.92	-45.18	Vela Pulsar
3390	09/20/94	14:49	10/04/94	12:22	W,T	234.71	-1.82	3C 317
4010	10/04/94	13:15	10/18/94	14:02	W,T	348.90	67.40	M 51
4020	10/18/94	15:15	10/25/94	14:07	W,T	211.71	-66.78	GAL 310-05
4025	10/25/94	14:55	11/01/94	14:07	W,T	202.34	-66.37	GAL 310-05
4030	11/01/94	15:26	11/09/94	13:38	N,T	254.46	35.34	HER X-1

Table 3—Continued

View Per.	Start Date	Start Time hh:mm	End Date	End Time hh:mm	Inst. Mode†	Z-Axis R.A. Deg.	Z-Axis Dec. Deg.	Target Region
4035	11/09/94	14:45	11/15/94	14:14	N,T	133.70	20.11	OJ 287
4040	11/15/94	15:32	11/29/94	14:11	W,T	354.98	-33.17	S Gal Pole
4050	11/29/94	15:27	12/13/94	14:21	W,T	194.93	-6.27	3C 279
4060	12/13/94	15:03	12/20/94	15:50	W,T	205.27	7.64	Virgo
4070	12/20/94	16:30	01/03/95	14:20	W,T	206.58	3.50	Virgo
4080	01/03/95	15:00	01/10/95	15:51	W,T	194.05	-5.79	3C 279
4090	01/10/95	16:52	01/24/95	16:06	W,T	68.52	-63.61	LMC
4100	01/24/95	17:11	02/14/95	15:54	W,T	337.33	18.83	GAL 082-33
4111	02/14/95	16:50	02/21/95	15:50	N,T	98.49	69.75	QSO 0716+714
4115	02/21/95	16:30	02/28/95	15:49	N,T	93.91	71.03	QSO 0716+714
4120	02/28/95	16:41	03/07/95	16:07	W,T	90.09	24.68	Gal Anticenter
4130	03/07/95	16:44	03/21/95	14:08	W,T	89.78	17.10	Gal Anitcenter
4143	03/29/95	14:23	04/04/95	14:04	W,T	257.28	-39.14	GRO J1655-40
4191	04/04/95	15:00	04/11/95	14:03	W,T	83.40	-3.84	Orion
4150	04/11/95	14:56	04/25/95	13:57	W,T	104.00	-65.30	LMC
4180	04/25/95	14:55	05/09/95	12:51	W,T	173.20	45.55	MRK 421
4195	05/09/95	14:53	05/23/95	15:13	W,T	86.68	-6.99	Orion
4200	05/23/95	15:55	06/06/95	16:31	W,T	79.91	4.12	Orion
4210	06/06/95	18:15	06/13/95	13:19	W,T	263.13	-32.68	Gal Center
4220	06/13/95	13:53	06/20/95	16:14	W,T	263.93	-33.02	Gal Center
4230	06/20/95	17:30	06/30/95	14:21	W,T	268.12	-26.82	Gal Center
4235	06/30/95	15:01	07/10/95	13:39	W,T	244.01	-31.94	Gal Center
4240	07/10/95	14:23	07/25/95	14:18	W,T	205.46	-42.88	CEN A
4250	07/25/95	14:48	08/08/95	14:07	W,T	22.90	14.43	GAL 137-47
4260	08/08/95	14:37	08/22/95	13:55	W,T	83.52	22.02	Gal Anticenter
4270	08/22/95	14:25	09/07/95	13:56	W,T	55.91	42.35	GAL 154-10
4280	09/07/95	14:31	09/20/95	12:57	W,T	17.68	-33.41	S Gal Pole
4290	09/20/95	13:32	09/27/95	14:12	W,T	272.51	-11.07	GAL 018+04
5010	10/03/95	13:44	10/17/95	12:55	N,T	277.41	-2.77	GAL 028+04
5020	10/17/95	13:25	10/31/95	14:14	N,T	81.92	13.85	PKS 0528+134
5060	11/07/95	14:14	11/14/95	13:59	W,T	343.55	65.12	CAS A-1
5030	11/14/95	14:11	11/21/95	15:33	W,T	337.80	55.63	CAS A-3
5040	11/21/95	15:43	11/28/95	15:05	W,T	353.94	51.11	CAS A-2
5070	11/28/95	15:35	12/08/95	00:38	N,T	338.15	11.73	CTA 102

Table 3—Continued

View Per.	Start Date	Start Time hh:mm	End Date	End Time hh:mm	Inst. Mode†	Z-Axis R.A. Deg.	Z-Axis Dec. Deg.	Target Region
5075	12/08/95	01:08	12/14/95	15:05	N,T	338.15	11.73	TOO
5080	12/14/95	15:35	12/20/95	15:32	N,T	270.27	-23.44	GAL 005+00
5090	12/20/95	15:53	01/02/96	14:18	N,T	265.99	-3.83	GAL 021+14
5100	01/02/96	15:12	01/05/96	13:45	N,T	114.67	-14.25	MONOCEROS
5105	01/05/96	13:53	01/16/96	15:33	N,T	113.47	-12.63	MONOCEROS
5110	01/16/96	15:57	01/30/96	15:15	N,T	190.75	0.07	3C 273
5115	01/30/96	15:45	02/06/96	15:00	N,T	197.49	-9.45	3C 279
5130	02/06/96	15:30	02/13/96	15:00	N,T	329.55	-30.30	PKS 2155-304
5150	02/20/96	15:43	03/05/96	15:00	N,T	187.83	32.76	QSO 1219+285
5170	03/05/96	15:20	03/18/96	15:00	N,T	34.57	-52.94	PKS 0208-512
5161	03/18/96	15:30	03/21/96	15:35	N,T	247.05	-40.75	GRO J1655-40
5165	03/21/96	16:32	04/03/96	14:17	N,T	250.24	38.00	MRK 501
5185	04/03/96	14:47	04/23/96	14:18	N,T	110.48	71.34	0716-714
5190	04/23/96	14:48	05/07/96	15:19	N,T	251.94	39.40	3C 345
5204	05/21/96	13:59	05/28/96	14:47	N,T	329.72	-30.23	PKS 2155-304
5210	05/28/96	15:27	06/11/96	12:43	N,T	74.34	-65.11	GRO J0516-609
5220	06/11/96	13:13	06/14/96	13:41	N,T	157.17	-59.51	CEN X-3
5260	07/30/96	14:47	08/13/96	13:46	N,T	87.38	20.53	GEMINGA
5270	08/13/96	14:16	08/20/96	15:05	N,T	90.27	19.34	CRAB Pulsar
5280	08/20/96	15:35	08/27/96	14:30	N,T	89.61	23.77	CRAB Pulsar
5295	08/27/96	15:35	09/06/96	13:54	N,T	253.50	-39.85	GRO J1655-40
5300	09/06/96	14:32	10/03/96	15:15	S,T	17.76	69.20	GRO J0004+73
5310	10/03/96	15:45	10/15/96	14:32	N,T	155.40	-57.44	PSR B1055-52
6011	10/15/96	15:16	10/29/96	13:58	N,T	312.28	25.63	PSR J2043+274
6060	12/10/96	15:52	12/17/96	15:02	N,T	194.80	-6.45	3C 279
6070	12/17/96	15:32	12/23/96	15:24	N,T	194.85	-6.39	3C 279
6080	12/23/96	15:54	12/30/96	15:09	N,T	194.99	-6.14	3C 279
6090	12/30/96	15:39	01/07/97	15:47	N,T	195.02	-6.03	3C 279
6100	01/07/97	16:17	01/14/97	15:25	N,T	195.02	-6.04	3C 279
6105	01/14/97	15:55	01/21/97	15:07	N,T	194.78	-3.94	3C 279
6111	01/21/97	15:37	01/28/97	14:46	N,T	195.04	-5.97	3C 279
6161	02/18/97	15:45	03/18/97	15:32	N,T	82.74	13.53	PKS 0528+134
6178	04/09/97	14:10	04/15/97	13:46	N,T	255.86	42.15	MRK 501
6215	06/17/97	13:53	06/24/97	14:05	N,T	192.18	-5.06	3C 279 TOO

Table 3—Continued

View Per.	Start Date	Start Time hh:mm	End Date	End Time hh:mm	Inst. Mode†	Z-Axis R.A. Deg.	Z-Axis Dec. Deg.	Target Region
6235	07/15/97	14:10	07/22/97	14:33	N,T	330.68	42.28	BL Lac
6250	08/05/97	14:04	08/19/97	13:37	N,T	266.46	-27.27	GRS 1758-258
6151	08/19/97	14:07	08/26/97	13:04	N,T	246.52	-29.85	PKS 1622-297
6270	09/02/97	14:15	09/09/97	13:11	N,T	164.38	-57.55	PKS 1055-52
6300	09/23/97	13:56	10/07/97	13:56	N,T	164.38	-57.55	PKS 1055-52
6311	11/03/97	15:00	11/11/97	15:17	N,T	39.66	16.62	PKS 0235+164
7010	11/11/97	15:47	11/18/97	14:44	N,T	331.66	-34.87	PKS 2155-304
7020	11/18/97	15:00	11/25/97	15:30	N,T	331.66	-34.87	PKS 2155-304
7080	12/30/97	15:31	01/06/98	14:27	N,T	331.66	-34.87	PKS 2155-304
7091	01/06/98	15:37	01/13/98	15:14	N,T	331.66	-34.87	PKS 2155-304
7100	01/13/98	16:04	01/21/98	14:25	N,T	269.96	57.44	2EG J1835+59
7110	01/21/98	14:35	01/27/98	15:34	N,T	269.96	57.44	2EG J1835+59
7155	03/20/98	17:00	03/27/98	15:18	N,T	180.13	31.23	1156+295
7165	03/27/98	15:48	04/02/98	18:04	N,T	162.80	40.60	MRK 421
7170	04/14/98	14:47	04/22/98	14:41	N,T	161.06	-63.06	CEN-X
7210	05/15/98	14:00	05/19/98	13:56	N,T	253.46	39.75	MRK 501
7225	05/22/98	15:00	05/27/98	14:16	N,T	253.46	39.75	MRK 501
7245	07/07/98	13:55	07/21/98	14:58	N,T	93.48	19.36	Geminga Psr.
7287	09/22/98	15:06	09/25/98	13:27	N,T	33.80	41.50	PSR 0218
7289	10/13/98	14:19	11/03/98	14:27	N,T	33.80	41.50	PSR 0218

†The instrument mode is designated by two letters. The first specifies the field of view, where W=wide field, N=narrow field, and S=strip mode. The second character specifies whether or not the the TASC is required in the triggering condition, where T=in coincidence and O=not in coincidence.

Note. — Information in this table was extracted from the EGRET timeline file that is available on-line from the Compton Observatory Science Support Center, currently at URL, ftp://cossc.gsfc.nasa.gov/pub/data/egret/timeline/timeline